Atom Interferometric Imaging of Differential Potentials Using an Atom Laser

M. E. Mossman,[1,2] Ryan A. Corbin,[2] Michael McNeil Forbes,[2,*] and P. Engels[2,†]
[1]Department of Physics and Biophysics, University of San Diego, San Diego, California 92110, USA
[2]Department of Physics and Astronomy, Washington State University, Pullman, Washington 99164, USA

(Received 12 August 2022; accepted 16 May 2023; published 28 June 2023)

Interferometry is a prime technique for modern precision measurements. Atoms, unlike light, have significant interactions with electric, magnetic, and gravitational fields, making their use in interferometric applications particularly versatile. Here, we demonstrate atom interferometry to image optical and magnetic potential landscapes over an area exceeding 240 μm × 600 μm. The differential potentials employed in our experiments generate phase imprints in an atom laser that are made visible through a Ramsey pulse sequence. We further demonstrate how advanced pulse sequences can enhance desired imaging features, e.g., to image steep potential gradients. A theoretical discussion is presented that provides a semiclassical analysis and matching numerics.

DOI: 10.1103/PhysRevLett.130.263402

Introduction.—From optical precision measurements [1] to detecting minute ripples in space-time [2], interferometry is a keystone of modern science. Compared to their light-based counterparts, matter-wave interferometers have some decisive advantages [3], including significant sensitivity to electric, magnetic, and gravitational fields [4–6]. Access to both motional and internal degrees of freedom makes atom interferometers suitable for many applications, including timekeeping with ultracold atoms [7], inertial measurements [8,9], and fundamental studies of quantum dynamics [10–13].

Here, we demonstrate the two-dimensional imaging of differential potentials based on atom interferometry with an atom laser—a coherent stream of atoms. Atom lasers [14–29] can be generated by coherently outcoupling atoms from a trapped dilute-gas Bose-Einstein condensate (BEC) into an untrapped quantum state, creating a two-dimensional sheet of atoms in an accelerated reference frame. Our interferometric imaging technique employs a Ramsey pulse sequence [30,31]: two sequential $\pi/2$ pulses, via coherent microwaves, separated by a wait time. The resulting images reveal contourlike lines of an applied differential potential. The potential causes a phase imprint that can be measured across the entire atom laser in a single run of the experiment, extending over an area exceeding 240 μm × 600 μm. Unlike previous atom interferometric work with a pulsed-output atom laser [32] or with thermal atoms [33], our work utilizes a quasicontinuous atom laser to map out two-dimensional potential landscapes. We demonstrate this technique with two types of differential potentials: a magnetic field that acts differently on two hyperfine states due to the Zeeman effect, and an optical dipole potential that is tuned to be attractive for one hyperfine state and repulsive for another.

As a practical application, we image a magnetic quadrupole field present in our experimental chamber, and show how a variation of the imaging pulse sequence can enhance desired features. Experimental results are well described by a semiclassical theory. Future applications include material science studies in hybrid quantum systems [34], studies of interaction effects in quantum caustics [35–37], and branched flow [38].

Experimental procedure and results.—Our experiments begin with a dilute-gas BEC of $\sim 4 \times 10^6$ atoms of ^{87}Rb in the $|F, m_F\rangle = |1, -1\rangle$ hyperfine state. The BEC is held in a hybrid trap formed by a focused infrared laser that provides mostly radial confinement, and a quadrupole magnetic field that provides additional support against gravity and axial confinement [Fig. 1(a)]. The resulting harmonic trap frequencies are $\{\omega_x, \omega_y, \omega_z\} = 2\pi \times \{3.7, 39.7, 30.1\}$ Hz, with the weakly confined x axis directed horizontally in the images. From this trapped BEC, a coherent stream of atoms is outcoupled to form an atom laser by using microwave radiation that gradually transfers atoms to the $|2, 0\rangle$ state, which is only weakly supported by the magnetic gradient. These transferred atoms fall out of the trap, accelerating downward from the injection site. After 10 ms of continuous outcoupling from the BEC, a brief 68 μs-long microwave pulse puts the entire atom laser into a coherent superposition of the $|2, 0\rangle$ and $|1, 0\rangle$ state.

The falling atoms can be further manipulated with a dipole potential created by impinging focused laser light that is detuned from a resonant transition. Under appropriate conditions, this can lead to strong mechanical effects such as intricate patterns of caustics [29]. The sign and strength of the dipole potential depend on the intensity and wavelength of the laser in relation to the resonance lines of the atom. Here, we exploit this versatility by choosing a

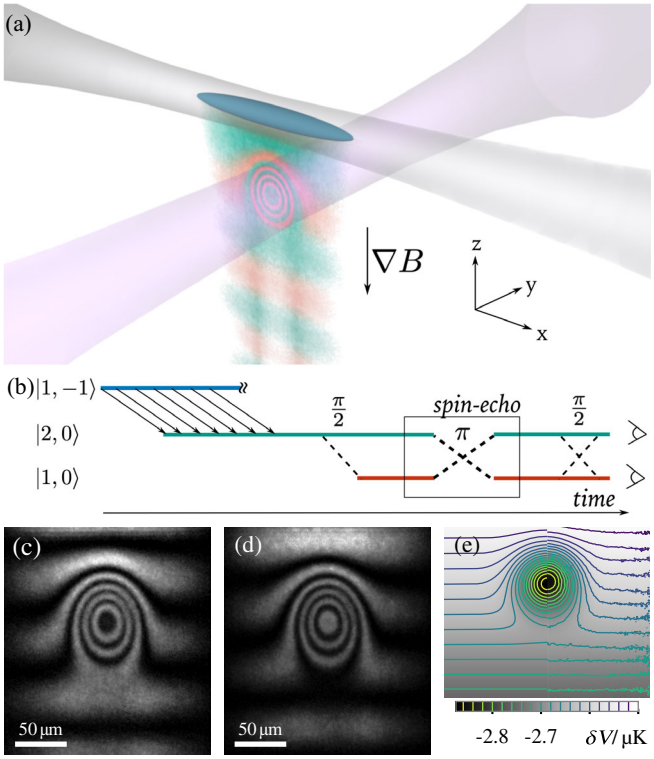

FIG. 1. (a) Experimental setup: a BEC (blue) of ^{87}Rb atoms in the $|F, m_F\rangle = |1, -1\rangle$ state is held in a dipole trap (gray). Atoms transferred to the $|2, 0\rangle$ state are accelerated out of the trap in the presence of gravity and a magnetic gradient, generating an atom laser that travels downward. An additional optical laser (violet) crosses the atom laser to generate weak differential potentials. (b) Interferometric imaging procedure. A first Ramsey pulse places the whole extent of the atom laser into a superposition state. Optionally, a π pulse can be inserted for realizing a spin echo. After a wait time, a second Ramsey pulse closes the interferometer with an arbitrary controllable phase, e.g., (c) $\theta = 0$ and (d) $\theta = \pi$. The images in (c) and (d) are taken with a Ramsey pulse spacing of 0.70 ms and have each been averaged over ten independent runs of the experiment. (e) By directly fitting the interference patterns (left), or with phase retrieval techniques (right), we can accurately reconstruct the differential potential $\delta V(x, z)$. See [39] for details.

laser wavelength such that the resulting potential is attractive for atoms in the $|1, 0\rangle$ state and repulsive for atoms in the $|2, 0\rangle$ state. See [39] for more details. The dipole potential focuses or defocuses the $|1, 0\rangle$ or $|2, 0\rangle$ atom lasers, respectively, and can in both cases form caustics for sufficiently high powers [29]. Here, we use weak dipole strengths that have only small mechanical effects on the atom laser, probing mostly the so-called "Aharonov-Bohm" phase [6]. The dipole is centered $z_d = 89.9(4)$ μm below the injection site, and the Gaussian waist radius of the dipole laser $w = 38.9(6)$ μm is smaller than the transverse extent of the atom laser (≈240 μm).

In addition to the dipole potential, a differential potential for atoms in the $|1, 0\rangle$ and $|2, 0\rangle$ states can be generated by a magnetic field, shifting their energies by the quadratic Zeeman effect. Here, with a background field of about 10 G and a vertical gradient of $dB/dz = -25.10(1)$ G/cm, the energy of the $|2, 0\rangle$ ($|1, 0\rangle$) state increases (decreases) with $h \times 12.43(6)$ kHz/mm in the $-z$ direction, determined using a linear approximation across the region of magnetic fields covered by the atom laser (see [39] for details). This magnetic field is present in the full region of the atom laser, whereas the dipole laser is focused to a region just below the trapped position of the BEC.

Atom interferometric imaging is performed by a Ramsey pulse sequence [Fig. 1(b)] followed directly by absorption imaging along the $-y$ direction with a 10 μs-long imaging pulse. The first 68 μs-long microwave $\pi/2$ pulse mentioned above creates a coherent superposition of the outcoupled $|1, 0\rangle$ and $|2, 0\rangle$ states. After an evolution time t_{wait}, a second 68 μs-long Ramsey pulse is applied to close the interferometer and apply an arbitrary phase shift. Because of the large hyperfine splitting of the ^{87}Rb ground state, atoms are imaged spin selectively.

In the presence of a differential potential, the phase evolution between the two Ramsey pulses leads to interference patterns observed in the spin-selective images. In Figs. 1(c), 1(d) and 2, this potential consists of the magnetic gradient along the vertical direction and [except in Fig. 2(a)] the dipole potential intersecting the atom laser. The differential potential was constant throughout the experiment, but switched off just before imaging. The magnetic potential leads to the observation of horizontal interference stripes [Fig. 2(a)], while the dipole potential causes the bull's-eye pattern seen in the upper part of the atom laser. For short pulse sequences, these approximate contour lines of the differential potential [see Eq. (7)]. Phase retrieval [47–49] or direct fitting techniques can be used to extract the potential shape, as demonstrated in Fig. 1(e).

In Fig. 2, the depth of the dipole potential is increased from panel to panel, increasing the number of interference rings in the bull's-eye pattern commensurate with the increased phase accumulation between the two Ramsey pulses. Matching numerics, shown in the left side of each panel in the figure, are in excellent agreement with the experimental images. Because of the low dipole laser intensities used in Fig. 2, the mechanical effects on the atom laser are small in the sense that no pronounced caustics are formed. For the $|2, 0\rangle$ state imaged in Fig. 2, the dipole potential is weakly repulsive, leading to a small but increasing suppression of the density in the region below the dipole laser as the power is increased.

Semiclassical analysis and quantitative comparison with experiment.—To theoretically treat our system, we approximate the physics using a semiclassical analysis [28,50,51]. To start, consider a system uniform along x, which is a good approximation near the center of our laser. Atoms are injected into the system at rest from the trapped cloud at

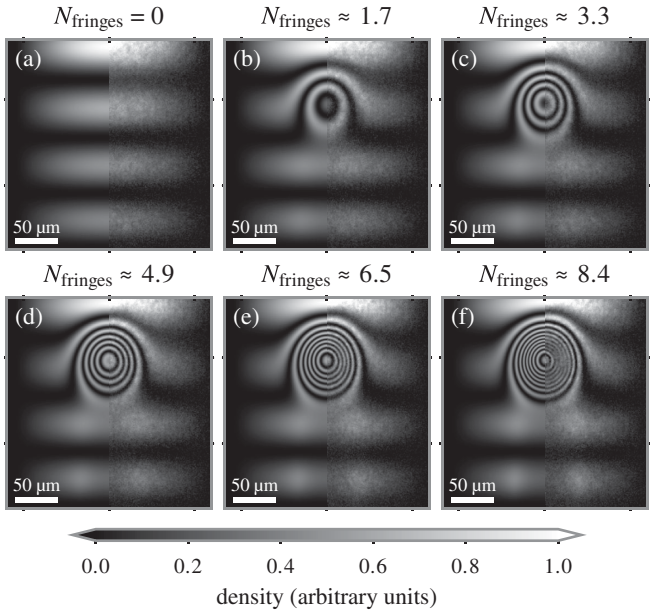

FIG. 2. Atom interferometric imaging of a combined magnetic and optical differential potential for several powers of the dipole potential. Each frame is split vertically and shows the theory result (left) compared to the experimental image (right). The experimental images were taken with a Ramsey pulse spacing of 0.5 ms and are averages of 30 experimental runs. The images show the atoms in the $|2,0\rangle$ state. The energy differences generated by the dipole beam between the $|2,0\rangle$ and $|1,0\rangle$ are (a) 0 μK, (b) 0.16(7) μK, (c) 0.32(6) μK, (d) 0.47(4) μK, (e) 0.6(2) μK, and (f) 0.81(7) μK, and are obtained with uncertainties by least-squares fitting of the experimental data with our model as described in [39]. Each title shows the expected number of fringes created by the dipole potential [Eq. (7)] estimated using the impulse approximation.

height $z = z_0$ and are immediately subject to a time-dependent potential $V(z,t)$ that includes both gravity and any external potentials, causing the atoms to fall. Atoms are continuously injected into the system, so atoms imaged at time t_i and height z_i will have been injected at some earlier time $t_0(t_i, z_i) \leq t_i$, which must be determined by solving the classical boundary-value problem:

$$m\ddot{z}(t) = -\frac{\partial}{\partial z} V(z(t), t), \tag{1a}$$

$$z(t_0) = z_0, \qquad \dot{z}(t_0) = 0, \qquad z(t_i) = z_i. \tag{1b}$$

We capture the effects of the various state transitions in the form of the potential $V(z,t)$: if a particle initially in the $|2,0\rangle$ state is subject to Ramsey pulse transition $|2,0\rangle \to (|2,0\rangle + |1,0\rangle)/\sqrt{2}$ at time t_1, then we must track two different classical trajectories, having the same potential $V(z,t)$ for $t < t_1$, but different species-dependent potentials $V_i(z,t)$ for later times.

In our analysis, we further assume $V(z_0,t) = 0$ for all times, such that the classical Hamiltonian at the injection site $H_0 = 0$, capturing the essence of coherence in the atom laser: injection occurs resonantly at a fixed energy, keeping the phase of the injected particles constant over time $\psi_0(z_0,t) = \psi_0(z_0)$.

The wave function follows from the path integral:

$$\psi(z,t) = \int dz_0 \int \mathcal{D}[q] \exp\left\{\frac{i}{\hbar} S[q]\right\} \psi(z_0, t_0), \tag{2a}$$

$$S[q] = \int_{t_0}^{t} dt \left(\frac{m\dot{q}^2}{2} - V(q(t), t)\right), \tag{2b}$$

where the integral is taken over all paths $q(t)$ subject to the boundary conditions $q(t) = z$ and $q(t_0) = z_0$, and $S[q]$ is the classical action. We assume highly localized injection $\psi(z_0, t_0) \propto \delta(z_0)$, which we take to be about $z_0 = 0$. (See [39] for details.)

The Wentzel-Kramers-Brillouin (WKB) approximation amounts to expanding the action

$$S[q + \xi] = S[q] + S'[q] \cdot \xi + \frac{1}{2!} S''[q] \cdot \xi\xi + \cdots \tag{3}$$

about the classical trajectories q_{cl} where $S'[q_{\text{cl}}] = 0$. Keeping only the quadratic fluctuations [50] with $S[q_{\text{cl}}] \equiv S(z, t; z_0, t_0)$,

$$\psi_{\text{WKB}}(z,t) = \int dz_0 \sqrt{\frac{-\partial^2 S/(2\pi i\hbar)}{\partial z \partial z_0}} e^{iS/\hbar} \psi(z_0, t_0). \tag{4}$$

If there are multiple trajectories that arrive at the same final position $z(t_i)$ at the time of imaging, one must add these amplitudes to obtain the appropriate interference pattern.

For this position-to-position transition,

$$\frac{\partial S}{\partial z} = p(t), \qquad \frac{\partial S}{\partial z_0} = -p(t_0), \quad \text{and} \quad \frac{\partial^2 S}{\partial z \partial z_0} = \frac{\partial p}{\partial z_0}. \tag{5}$$

If the force is conservative, $E = p^2/2m + V(z) = p_0^2/2m + V(z_0)$ and one recovers the familiar factor of $\sqrt{p}$ in the denominator of $\psi_{\text{WKB}}(z,t)$:

$$p(z_0, t_0) = -\sqrt{p_0^2 + 2m(V(z_0) - V(z))}, \qquad \frac{\partial p}{\partial z_0} \propto \frac{1}{p}. \tag{6}$$

The semiclassical problem is thus reduced to solving for the classical trajectories of particles injected at $q(t_0) = (x_0, z_0)$ that end up at $q(t_i) = (x, z) \equiv \vec{x}$ in the image.

When preparing numerical simulations for the experiment, we interfere two different trajectories: those of the particles which remain in state $|2,0\rangle$ (ψ_1) and those which start in the state $|2,0\rangle$ but are converted to state $|1,0\rangle$ for times between the two Ramsey pulses (ψ_2). This procedure has a few deficiencies. First, the semiclassical amplitudes diverge at the turning point $z = z_0$. This can be remedied by

using Airy functions, but to demonstrate the accuracy of the pure semiclassical calculation, we simply exclude the region close to the injection site in our comparisons. Second, the model assumes instantaneous state transitions. We mitigate this by allowing the transition to occur at a time slightly shifted from the middle of the transition window that accounts for the acceleration of the particles. A proper semiclassical accounting for this effect requires a multicomponent WKB approximation [52–55], which is much more complicated and not needed here.

The interference pattern $I_n \propto |\psi_1 + \psi_2|^2$ can be modeled as $I_n(\vec{x}) \approx a(\vec{x}) + b(\vec{x})\cos(\phi(\vec{x}) + \theta_n)$ where θ_n is an experimentally controllable phase. Phase retrieval techniques [47–49] can efficiently extract the difference in actions between the paths $\hbar\phi(\vec{x}) = S_1(\vec{x}) - S_2(\vec{x}) + \text{const}$, from which the differential potential can be extracted. This requires imaging at least three different values of θ_n (see [39]).

Alternatively, if the form of the potential is known up to a few parameters, then the interference pattern can be directly modeled from a single value of θ_n, allowing high-precision fitting of these parameters. This analysis is the basis for our numerical simulations and leads to a quantitative explanation of the experimental data, as demonstrated in Fig. 2. With a few simplifying approximations that we call the "impulse approximation"—assuming weak potentials do not appreciably deflect the particles, and the transitions and t_{wait} are sufficiently fast such that the particles do not fall significantly during the Ramsey pulse sequence—one obtains the following density pattern, and corresponding expected number of maxima (fringes) in the interference pattern:

$$n_{2,0}^{\text{Ramsey}} \propto 1 - \cos\left(\frac{t_{\text{wait}}}{\hbar}\delta V\right), \qquad N_{\text{fringes}} \approx \frac{t_{\text{wait}}\delta V_{\text{max}}}{2\pi\hbar}, \tag{7}$$

where δV_{max} is the maximum of the differential potential $\delta V(\vec{x})$ (see also [39]). This agrees well with the full calculations and experiments, as shown in Fig. 2.

Magnetic field mapping.—So far, we have demonstrated the effect of combined magnetic and optical differential potentials using Ramsey pulse sequences between the $|2,0\rangle$ and $|1,0\rangle$ states. This transition is only weakly sensitive to magnetic fields due to second order Zeeman effects. In applications where a greater sensitivity to magnetic fields is desired, a strongly magnetic field dependent transition such as the one between the stretched states $|1,-1\rangle$ and $|2,-2\rangle$ can be employed. In ^{87}Rb, this transition shifts by -2.1 MHz/G in low fields, compared to 11 kHz/G for the $|1,0\rangle$ to $|2,0\rangle$ transition in a bias field of 10 G. When using magnetically sensitive transitions, care must be taken that the Ramsey pulses affect the entire atom laser, otherwise a state transfer will occur in only a small region, which can be used for fluid flow tracing [29].

We demonstrate the capability of using the $|1,-1\rangle$ to $|2,-2\rangle$ transition to detect small magnetic gradient fields in Fig. 3. Here, an atom laser is generated from a BEC confined in a purely optical trap: a large-diameter dipole beam is employed to provide mostly radial confinement, and two repulsive, thin dipole sheets are added as "end caps" on the left and right side of the BEC to provide axial confinement. The atom laser is then realized by ramping down the intensity of the large-diameter dipole beam to create a wide atom laser without relying on any preexisting magnetic gradient for the output coupling. To generate a test pattern, a magnetic quadrupole field with an axial gradient of 140(10) mG/cm was added, approximately 2 orders of magnitude smaller than the gradient used for the previous images. The position of the quadrupole field zero was adjusted relative to the imaging window using small magnetic bias fields, as shown schematically in Fig. 3(d). The results clearly show the tilt of the equipotential lines in the magnetic quadrupole field, demonstrating the capability of imaging magnetic field gradients in a single experimental run.

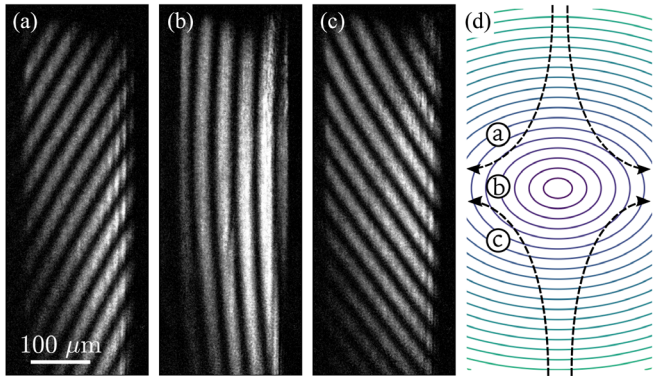

FIG. 3. Atom interferometric fringe pattern using the magnetically sensitive transition between $|1,-1\rangle$ and $|2,-2\rangle$. A magnetic quadrupole field with gradient $dB/dz = 140(10)$ mG/cm was placed with its center to the right and (a) slightly below, (b) right next to, and (c) slightly above the atom laser. The Ramsey pulses are spaced by 2 ms. The images show the atoms detected in the $|2,-2\rangle$ state after the Ramsey sequence. Each image is from a single repetition of the experiment. (d) Schematic representation of quadrupole field (not to scale). Letters correspond to panels (a) to (c) and indicate the position of quadrupole field. The magnetic gradient has been calculated from the interference pattern in panel (b).

Spin-echo imaging.—Atom interferometric techniques provide great flexibility for the design of experimental sequences. While the experiments described above have all used a Ramsey pulse sequence, extended sequences can be employed to enhance specific features. One example is demonstrated in Fig. 4 where the Ramsey sequence has been augmented by inserting an additional π pulse, realizing a spin-echo sequence. Such a sequence can be used to cancel the effects of constant differential potentials and to produce contour lines of the gradient along the direction of motion. For Fig. 4(a), a pulse spacing t_{wait} of 1504 μs between the two pulses of a Ramsey sequence was used,

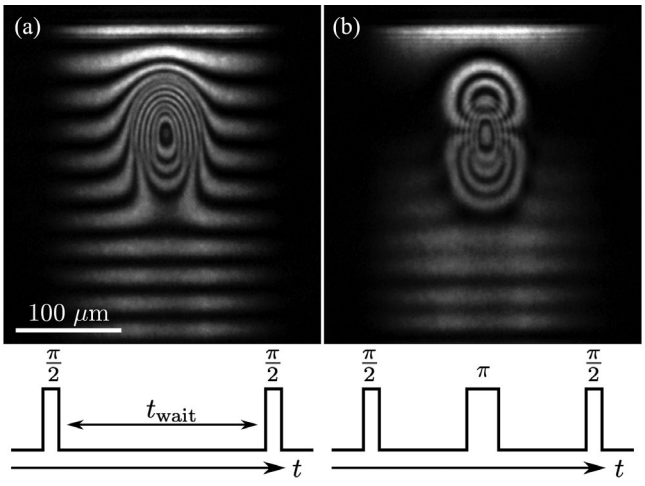

FIG. 4. Comparison of (a) Ramsey imaging and (b) spin-echo imaging. Pulse sequence timelines are depicted below each image (not drawn to scale). Both images show the $|2,0\rangle$ state 0.5 ms after the end of the pulse sequence. Total wait time between the $\pi/2$ pulses is $t_{\mathrm{wait}} = 1504$ μs in both cases. Images have been averaged over 30 independent experimental runs of the same parameters.

with each $\pi/2$ pulse lasting 53 μs and connecting the $|2,0\rangle$ and $|1,0\rangle$ states. The corresponding spin-echo sequence shown in Fig. 4(b) was chosen to have the same total length of the sequence between the Ramsey pulses. The two panels in Fig. 4 show that, over a significant region in the upper part of the atom laser, the spin-echo sequence suppresses the horizontal stripes caused by the weak magnetic gradient, while imaging the gradient of the dipole potential along the vertical direction. The oval-shaped features in the center of Fig. 4(b) are a consequence of an inefficiency of the π pulse in the center of the potential where light shifts are significant. Similarly, the cancellation of the horizontal stripe pattern near the bottom of the image is incomplete as the π pulse is slightly shifted out of resonance here. In principle, these issues could be mitigated if sufficient microwave power is available by applying shorter pulses with larger linewidths. This demonstrates the capabilities of suitably chosen pulse sequences to enhance or modify the imaging contrast of desired features.

Conclusion.—As demonstrated in this work, atom interferometric imaging with an atom laser is a powerful tool for detecting and evaluating differential potentials over a large two-dimensional area. With the availability of highly tunable pulse sequences and several accessible spin states for measuring a variety of differential potentials, this technique is highly versatile and can be adapted for a wide set of applications. As an applied example, relating to work presented in Ref. [34], one can consider applications to material science where a material under study is placed parallel to the sheet of an atom laser, detecting the magnetic fields emanating from the material by imaging them in the plane of the atom laser using the interferometric technique.

P. E. acknowledges support from the National Science Foundation (NSF) through Grant No. PHY-1912540 and from the Ralph G. Yount Distinguished Professorship at WSU. M. E. M. acknowledges support from the NSF through Grant No. PHY-2137848 and from the Clare Boothe Luce Professorship Program of the Henry Luce Foundation. R. A. C. and M. M. F. acknowledge support from the NSF under Grant No. PHY-2012190.

*m.forbes@wsu.edu
†engels@wsu.edu

[1] S. Yang and G. Zhang, A review of interferometry for geometric measurement, Meas. Sci. Technol. **29**, 102001 (2018).
[2] B. P. Abbott *et al.* (LIGO Scientific, Virgo Collaborations), GW151226: Observation of Gravitational Waves from a 22-Solar-Mass Binary Black Hole Coalescence, Phys. Rev. Lett. **116**, 241103 (2016).
[3] K. Bongs, M. Holynski, J. Vovrosh, P. Bouyer, G. Condon, E. Rasel, C. Schubert, W. P. Schleich, and A. Roura, Taking atom interferometric quantum sensors from the laboratory to real-world applications, Nat. Rev. Phys. **1**, 731 (2019).
[4] N. Robins, P. Altin, J. Debs, and J. Close, Atom lasers: Production, properties and prospects for precision inertial measurement, Phys. Rep. **529**, 265 (2013).
[5] G. Rosi, F. Sorrentino, L. Cacciapuoti, M. Prevedelli, and G. M. Tino, Precision measurement of the Newtonian gravitational constant using cold atoms, Nature (London) **510**, 518 (2014).
[6] C. Overstreet, P. Asenbaum, J. Curti, M. Kim, and M. A. Kasevich, Observation of a gravitational Aharonov-Bohm effect, Science **375**, 226 (2022).
[7] A. D. Cronin, J. Schmiedmayer, and D. E. Pritchard, Optics and interferometry with atoms and molecules, Rev. Mod. Phys. **81**, 1051 (2009).
[8] S. Abend, M. Gersemann, C. Schubert, D. Schlippert, E. M. Rasel, M. Zimmermann, M. A. Efremov, A. Roura, F. A. Narducci, and W. P. Schleich, Atom interferometry and its applications, in *Foundations of Quantum Theory*, in Proceedings of the International School of Physics "Enrico Fermi" Vol. 197, edited by E. M. Rasel, W. P. Schleich, and S. Wölk (IOS Press, Amsterdam, 2019), pp. 345–392, 10.3254/978-1-61499-937-9-345.
[9] B. Stray, A. Lamb, A. Kaushik, J. Vovrosh, A. Rodgers, J. Winch, F. Hayati, D. Boddice, A. Stabrawa, A. Niggebaum, M. Langlois, Y.-H. Lien, S. Lellouch, S. Roshanmanesh, K. Ridley, G. de Villiers, G. Brown, T. Cross, G. Tuckwell, A. Faramarzi, N. Metje, K. Bongs, and M. Holynski, Quantum sensing for gravity cartography, Nature (London) **602**, 590 (2022).
[10] S. Moulder, S. Beattie, R. P. Smith, N. Tammuz, and Z. Hadzibabic, Quantized supercurrent decay in an annular Bose-Einstein condensate, Phys. Rev. A **86**, 013629 (2012).
[11] L. Corman, L. Chomaz, T. Bienaimé, R. Desbuquois, C. Weitenberg, S. Nascimbène, J. Dalibard, and J. Beugnon, Quench-Induced Supercurrents in an Annular Bose Gas, Phys. Rev. Lett. **113**, 135302 (2014).

[12] S. Eckel, F. Jendrzejewski, A. Kumar, C. Lobb, and G. Campbell, Interferometric Measurement of the Current-Phase Relationship of a Superfluid Weak Link, Phys. Rev. X **4**, 031052 (2014).
[13] G. Del Pace, K. Xhani, A. M. Falconi, M. Fedrizzi, N. Grani, D. H. Rajkov, M. Inguscio, F. Scazza, W. J. Kwon, and G. Roati, Imprinting persistent currents in tunable fermionic rings, Phys. Rev. X **12**, 041037 (2023).
[14] M.-O. Mewes, M. R. Andrews, D. M. Kurn, D. S. Durfee, C. G. Townsend, and W. Ketterle, Output Coupler for Bose-Einstein Condensed Atoms, Phys. Rev. Lett. **78**, 582 (1997).
[15] M. Naraschewski, A. Schenzle, and H. Wallis, Phase diffusion and the output properties of a cw atom-laser, Phys. Rev. A **56**, 603 (1997).
[16] W. Ketterle and H.-J. Miesner, Coherence properties of Bose-Einstein condensates and atom lasers, Phys. Rev. A **56**, 3291 (1997).
[17] H. Steck, M. Naraschewski, and H. Wallis, Output of a Pulsed Atom Laser, Phys. Rev. Lett. **80**, 1 (1998).
[18] I. Bloch, T. W. Hänsch, and T. Esslinger, Atom Laser with a cw Output Coupler, Phys. Rev. Lett. **82**, 3008 (1999).
[19] J. Schneider and A. Schenzle, Output from an atom laser: Theory vs. experiment, Appl. Phys. B **69**, 353 (1999).
[20] R. J. Ballagh and C. M. Savage, The theory of atom lasers, Mod. Phys. Lett. B **14**, 153 (2000).
[21] I. Bloch, T. W. Hänsch, and T. Esslinger, Measurement of the spatial coherence of a trapped Bose gas at the phase transition, Nature (London) **403**, 166 (2000).
[22] Y. L. Coq, J. H. Thywissen, S. A. Rangwala, F. Gerbier, S. Richard, G. Delannoy, P. Bouyer, and A. Aspect, Atom Laser Divergence, Phys. Rev. Lett. **87**, 170403 (2001).
[23] I. Bloch, M. Köhl, M. Greiner, T. W. Hänsch, and T. Esslinger, Optics with an Atom Laser Beam, Phys. Rev. Lett. **87**, 030401 (2001).
[24] A. P. Chikkatur, Y. Shin, A. E. Leanhardt, D. Kielpinski, E. Tsikata, T. L. Gustavson, D. E. Pritchard, and W. Ketterle, A continuous source of Bose-Einstein condensed atoms, Science **296**, 2193 (2002).
[25] S. A. Haine, J. J. Hope, N. P. Robins, and C. M. Savage, Stability of Continuously Pumped Atom Lasers, Phys. Rev. Lett. **88**, 170403 (2002).
[26] G. M. Lee, S. A. Haine, A. S. Bradley, and M. J. Davis, Coherence and linewidth of a continuously pumped atom laser at finite temperature, Phys. Rev. A **92**, 013605 (2015).
[27] G. Harvie, A. Butcher, and J. Goldwin, Coherence time of a cold-atom laser below threshold, Opt. Lett. **45**, 5448 (2020).
[28] J.-F. Riou, Y. Le Coq, F. Impens, W. Guerin, C. J. Bordé, A. Aspect, and P. Bouyer, Theoretical tools for atom-laser-beam propagation, Phys. Rev. A **77**, 033630 (2008).
[29] M. E. Mossman, T. M. Bersano, M. M. Forbes, and P. Engels, Gravitational caustics in an atom laser, Nat. Commun. **12**, 7226 (2021).
[30] N. F. Ramsey, A molecular beam resonance method with separated oscillating fields, Phys. Rev. **78**, 695 (1950).
[31] B. H. Bransden and C. J. Joachain, *Physics of Atoms and Molecules* (Prentice Hall, Harlow, England; New York, 2003).
[32] D. Döring, J. E. Debs, N. P. Robins, C. Figl, P. A. Altin, and J. D. Close, Ramsey interferometry with an atom laser, Opt. Express **17**, 20661 (2009).
[33] G. Ramola, R. Winkelmann, K. Chandrashekara, W. Alt, P. Xu, D. Meschede, and A. Alberti, Ramsey Imaging of Optical Traps, Phys. Rev. Appl. **16**, 024041 (2021).
[34] S. Taylor, F. Yang, B. A. Freudenstein, and B. Lev, A scanning quantum cryogenic atom microscope at 6 K, SciPost Phys. **10**, 060 (2021).
[35] D. H. J. O'Dell, Quantum Catastrophes and Ergodicity in the Dynamics of Bosonic Josephson Junctions, Phys. Rev. Lett. **109**, 150406 (2012).
[36] J. Mumford, W. Kirkby, and D. H. J. O'Dell, Catastrophes in non-equilibrium many-particle wave functions: Universality and critical scaling, J. Phys. B **50**, 044005 (2017).
[37] J. Mumford, E. Turner, D. W. L. Sprung, and D. H. J. O'Dell, Quantum Spin Dynamics in Fock Space following Quenches: Caustics and Vortices, Phys. Rev. Lett. **122**, 170402 (2019).
[38] E. J. Heller, R. Fleischmann, and T. Kramer, Branched flow, Phys. Today **74**, No. 12, 44 (2021).
[39] See Supplemental Material at http://link.aps.org/supplemental/10.1103/PhysRevLett.130.263402 for details about the numerical calculations, and a derivation of formula Eq. (7) under the impulse approximation, which includes Refs. [40–46].
[40] B. Deissler, K. J. Hughes, J. H. T. Burke, and C. A. Sackett, Measurement of the ac Stark shift with a guided matter-wave interferometer, Phys. Rev. A **77**, 031604 (2008).
[41] T. Kramer and M. Rodríguez, Quantum theory of an atom laser originating from a Bose-Einstein condensate or a Fermi gas in the presence of gravity, Phys. Rev. A **74**, 013611 (2006); **75**, 069905(E) (2007).
[42] K. Härkönen, O. Vainio, and K.-A. Suominen, Wave-packet analysis of interference patterns in output coupled atoms, Phys. Rev. A **81**, 043638 (2010).
[43] C. Bracher, W. Becker, G. S. A., M. Kleber, and M. S. Marinov, Three-dimensional tunneling in quantum ballistic motion, Am. J. Phys. **66**, 38 (1998).
[44] O. Vallée and M. Soares, *Airy Functions and Applications to Physics*, 2nd ed. (Imperial College Press, London, 2010).
[45] N. Robins, C. Savage, and E. A. Ostrovskaya, Atom-laser dynamics, Phys. Rev. A **64**, 043605 (2001).
[46] M. Edwards, D. A. Griggs, P. L. Holman, C. W. Clark, S. L. Rolston, and W. D. Phillips, Properties of a Raman atom-laser output coupler, J. Phys. B **32**, 2935 (1999).
[47] J. H. Bruning, D. R. Herriott, J. E. Gallagher, D. P. Rosenfeld, A. D. White, and D. J. Brangaccio, Digital wavefront measuring interferometer for testing optical surfaces and lenses, Appl. Opt. **13**, 2693 (1974).
[48] R. Juarez-Salazar, C. Mendoza-Rodriguez, J. E. Hernandez-Beltran, and C. Robledo-Sanchez, How do phase-shifting algorithms work?, Eur. J. Phys. **39**, 065302 (2018).
[49] J. Schwiegerling, *Optical Specification, Fabrication, and Testing*, 1st ed. (SPIE–The International Society for Optical Engineering, Bellingham, 2014).
[50] P. Cartier and C. DeWitt-Morette, *Functional Integration: Action and Symmetries*, Cambridge Monographs on Mathematical Physics (Cambridge University Press, Cambridge, 2006).
[51] T. A. Zapata and S. A. Fulling, WKB propagators in position and momentum space for a linear potential with a 'ceiling' boundary, J. Phys. A **50**, 105303 (2017).

[52] W. van Dijk and M. Razavy, Exact and Glauber amplitudes in multi-channel scattering, Can. J. Phys. **57**, 1952 (1979).
[53] R. G. Littlejohn and W. G. Flynn, Geometric phases in the asymptotic theory of coupled wave equations, Phys. Rev. A **44**, 5239 (1991).
[54] C. Emmrich and H. Römer, Multicomponent WKB and quantization, Acta Phys. Pol. B **27**, 2393 (1996).
[55] K. Hagino and A. B. Balantekin, WKB approximation for multichannel barrier penetrability, Phys. Rev. A **70**, 032106 (2004).